INSTITUTE OF PHYSICS
SERIES IN MATERIALS
SCIENCE AND ENGINEERING

HIGH-κ GATE DIELECTRICS

EDITED BY
M HOUSSA

IoP

High-k Gate Dielectrics edited by Michel Houssa

ISBN 0 7503 0906 7

Chapter 4.5

Ab initio calculations of the structural, electronic and dynamical properties of high-κ dielectrics

Gian-Marco Rignanese, Xavier Gonze and Alfredo Pasquarello

Introduction

The accurate prediction of materials properties is one of the pivotal goals of computational condensed matter physics. In this framework, the density functional theory (DFT) has emerged as an extremely successful approach. The success of DFT not only encompasses standard bulk materials but also complex systems such as proteins and carbon nanotubes.

In the framework of the quest for an alternative high-κ material to conventional SiO_2 as the gate dielectric in MOS devices, first-principles calculations can provide insight into the nanoscopic behaviour of novel materials without requiring empirical data. This is particularly relevant for the early stages of research when relatively few experimental data are available. DFT is appropriate to study ground state properties of the electronic system. In this chapter, we focus on structural, vibrational and dielectric properties, which all relate to the ground state of the electronic system and are thus well described within DFT.

Despite its predictive accuracy, DFT calculations have one important limitation associated with their high computational cost, which limits both the length and time scales of the phenomena which can be modelled. With the most widespread DFT approach based on plane-wave basis sets and pseudopotentials, it is currently possible to treat systems containing up to hundreds of atoms. For our application to high-κ materials, it is important to note that materials containing transition-metal and first-row elements (e.g. oxygen) generally present an additional difficulty when treated with plane-wave basis sets. In fact, their valence wave functions are generally strongly localized around the nucleus and may require a large number of basis functions to be described accurately, thus further limiting the size of the system that can be investigated.

This chapter is dedicated to the first-principles study of the Hf–Si–O and Zr–Si–O systems which have drawn considerable attention as alternative high-κ materials. Indeed, the metal oxides HfO_2 and ZrO_2 as well as the silicates $HfSiO_4$ and $ZrSiO_4$ in the form of amorphous films are stable in direct contact with Si up to high temperature, which is highly desirable to avoid the degradation of the interface properties by formation of a low-κ interfacial layer. In fact, the Hf–Si–O and Zr–Si–O phase diagrams present a large phase field of stable silicates and the static permittivity ϵ_0 increases continuously with the amount of Hf and Zr incorporated into the silicate film. In order to be able to control this process, it is highly desirable to develop an understanding of how the permittivities of Hf and Zr silicates are affected by the underlying nanoscopic structure.

This chapter is organized as follows. In the 'Theoretical background' section, we present a brief summary of the DFT and the equations related to the properties that will be presented in the subsequent sections. We also give some technical details about the calculations. The 'Crystalline oxides' section is dedicated to the study of structural, vibrational and dielectric properties of hafnia (HfO_2) and zirconia (ZrO_2). Both the cubic and tetragonal phases are considered. The differences and the analogies between the two phases and between hafnia and zirconia are highlighted. In the 'Crystalline silicates' section, we present structural and electronic properties of hafnon ($HfSiO_4$) and zircon ($ZrSiO_4$). We compare their Born effective charge tensors and discuss the phonon frequencies at the Γ point. The dielectric permittivity tensors are analysed in detail. The fifth section is devoted to the study of amorphous silicates. We introduce a scheme which relates the dielectric constants to the local bonding of Si and $M = (Hf, Zr)$ atoms. This scheme is based on the definition of parameters characteristic of the basic structural units (SUs) formed by Si and $M = (Hf, Zr)$ atoms and their nearest neighbours, and allows us to avoid heavy large-scale calculations, which are beyond current computational capabilities. Applied to amorphous Zr silicates, our scheme provides a good description of the measured dielectric constants, both of the optical and the static ones. Finally, in the last section, we give the conclusions.

Theoretical background

Ground state properties

The main idea of DFT is to describe an interacting system of fermions through the electron density rather than through the many-body wave function. For N electrons in a solid obeying the Pauli principle and interacting via the Coulomb potential, this means that the basic variable of the system depends only on three (the spatial coordinates x, y and z) rather than $3N$ degrees of freedom.

In 1964, Hohenberg and Kohn [1] demonstrated that the ground state of the electron system is defined by the electron density which minimizes the total energy. Furthermore, they showed that all the other ground state properties of the system (e.g. the lattice constant, the cohesive energy, etc) are functionals of the ground state electron density. This means that, once the ground state electron density is known, all the other ground state properties follow (in principle, at least).

In 1965, Kohn and Sham [2] showed that this variational approach leads to equations of a very simple form:

$$(T + v_{\mathrm{KS}}[n])|\psi_\alpha\rangle = (T + v_{\mathrm{ext}} + v_{\mathrm{H}}[n] + v_{\mathrm{xc}}[n])|\psi_\alpha\rangle = \epsilon_\alpha|\psi_\alpha\rangle, \tag{4.5.1}$$

nowadays known as the Kohn–Sham equations. These effectively single-particle eigenvalue equations are similar in form to the time-independent Schroedinger equation, T being the kinetic energy operator and v_{KS} the potential experienced by the electrons. The latter is generally split into a part which is external to the electronic system v_{ext}, for instance the electron–ion interaction, and a part describing the electron–electron interactions. For convenience, the latter is further split into the Hartree potential v_{H} and the exchange–dcorrelation potential v_{xc}, whose form is, in general, unknown.

The ground state energy of the electronic system is given by:

$$E_{\mathrm{el}}\{\psi_\alpha\} = \sum_{\alpha}^{\mathrm{occ}} \langle\psi_\alpha|T + v_{\mathrm{ext}}|\psi_\alpha\rangle + E_{\mathrm{Hxc}}[n], \tag{4.5.2}$$

where E_{Hxc} is the Hartree and exchange–correlation energy functional of the electron density $n(\mathbf{r})$ with $\delta E_{\mathrm{Hxc}}/\delta n = v_{\mathrm{H}} + v_{\mathrm{xc}}$, and the summation runs over the occupied states α. The occupied Kohn–Sham orbitals are subject to the orthonormalization constraints,

$$\int \psi_\alpha^*(\mathbf{r})\psi_\beta(\mathbf{r})\,\mathrm{d}\mathbf{r} = \langle\psi_\alpha|\psi_\beta\rangle = \delta_{\alpha\beta}, \tag{4.5.3}$$

where α and β label occupied states. The density is generated from

$$n(\mathbf{r}) = \sum_{\alpha}^{\mathrm{occ}} \psi_\alpha^*(\mathbf{r})\psi_\alpha(\mathbf{r}). \tag{4.5.4}$$

Nowadays, DFT is considered as the method of choice for simulating solids and molecules from first principles. For a review of DFT applications, we recommend the article of Pickett [3]. The interested reader may find more technical details about DFT in the review article of Payne *et al* [4].

Response properties

In this brief presentation, we focus on the *responses* of solid systems to two classes of perturbations: (a) collective displacements of atoms characterized by a wavevector $\mathbf{q}$ (phonons) and (b) homogeneous static electric fields. These responses can also be calculated within DFT using various methods, as reviewed by Baroni *et al* [5].

The method that we adopt in the calculations presented here relies on a variational approach to density-functional perturbation theory: a complete description can be found in [6, 7]. The first paper [6] describes the computation of the first-order derivatives of the wave functions, density and self-consistent potential with respect to the perturbations mentioned above; while the second paper [7] is dedicated to the second-order derivatives. We adopt the same notations as in those references to introduce the properties that are studied in the subsequent sections. In particular, κ and α run over the atoms in the unit cell and over the three Cartesian directions, respectively; $\tau_{\kappa\alpha}$ denote the equilibrium positions.

The squares of the phonon frequencies $\omega^2_{m\mathbf{q}}$ at $\mathbf{q}$ are obtained as eigenvalues of the dynamical matrix $\tilde{D}_{\kappa\alpha,\kappa'\beta}(\mathbf{q})$, or as solutions of the following generalized eigenvalue problem:

$$\sum_{\kappa'\beta} \tilde{C}_{\kappa\alpha,\kappa'\beta}(\mathbf{q}) U_{m\mathbf{q}}(\kappa'\beta) = M_\kappa \omega^2_{m\mathbf{q}} U_{m\mathbf{q}}(\kappa\alpha), \tag{4.5.5}$$

where M_κ is the mass of the ion κ, and the matrix $\tilde{C}$ is connected to the dynamical matrix $\tilde{D}$ through:

$$\tilde{D}_{\kappa\alpha,\kappa'\beta}(\mathbf{q}) = \tilde{C}_{\kappa\alpha,\kappa'\beta}(\mathbf{q})/(M_\kappa M_{\kappa'})^{1/2}. \tag{4.5.6}$$

The matrix $\tilde{C}_{\kappa\alpha,\kappa'\beta}(\mathbf{q})$ is the Fourier transform of the matrix of the interatomic force constants. It is related to the second-order derivative of the total energy with respect to collective atomic displacements [7].

The limit $\mathbf{q} \rightarrow \mathbf{0}$ must be performed carefully [7] by the separate treatment of the macroscopic electric field associated with phonons in this limit. A bare dynamical matrix at $\mathbf{q} = \mathbf{0}$ is first computed, then a non-analytical part is added, in order to reproduce correctly the $\mathbf{q} \rightarrow \mathbf{0}$ behaviour along different directions:

$$\tilde{C}_{\kappa\alpha,\kappa'\beta}(\mathbf{q} \rightarrow \mathbf{0}) = \tilde{C}_{\kappa\alpha,\kappa'\beta}(\mathbf{q} = \mathbf{0}) + \tilde{C}^{\mathrm{NA}}_{\kappa\alpha,\kappa'\beta}(\mathbf{q} \rightarrow \mathbf{0}). \tag{4.5.7}$$

The expression of the non-analytical part will be given later on in this section.

For insulators, the dielectric permittivity tensor is the coefficient of proportionality between the macroscopic displacement field and the macroscopic electric field, in the linear regime:

$$\mathcal{D}_{\text{mac},\alpha} = \sum_{\beta} \epsilon_{\alpha\beta} \mathcal{E}_{\text{mac},\beta}. \tag{4.5.8}$$

It can be obtained as

$$\epsilon_{\alpha\beta} = \frac{\partial \mathcal{D}_{\text{mac},\alpha}}{\partial \mathcal{E}_{\text{mac},\beta}} = \delta_{\alpha\beta} + 4\pi \frac{\partial \mathcal{P}_{\text{mac},\alpha}}{\partial \mathcal{E}_{\text{mac},\beta}}. \tag{4.5.9}$$

In general, the displacement $\mathcal{D}_{\text{mac}}$, or the polarization $\mathcal{P}_{\text{mac}}$, will include contributions from ionic displacements. In the presence of an applied field of high frequency, the contribution to the dielectric permittivity tensor resulting from the electronic polarization, usually denoted $\epsilon^{\infty}_{\alpha\beta}$, dominates. This ion-clamped dielectric permittivity tensor is related to the second-order derivatives of the energy with respect to the macroscopic electric field [7]. Later on in this section, we will consider the supplementary contributions to the polarization coming from the ionic displacements.

For insulators, the Born effective charge tensor $Z^{*}_{\kappa,\beta\alpha}$ is defined as the proportionality coefficient relating, at linear order, the polarization per unit cell, created along the direction β, and the displacement along the direction α of the atoms belonging to the sublattice κ, under the condition of zero electric field. The same coefficient also describes the linear relation between the force on an atom and the macroscopic electric field:

$$Z^{*}_{\kappa,\beta\alpha} = \Omega_0 \frac{\partial \mathcal{P}_{\text{mac},\beta}}{\partial \tau_{\kappa\alpha}(\mathbf{q}=\mathbf{0})} = \frac{\partial F_{\kappa,\alpha}}{\partial \mathcal{E}_{\beta}}, \tag{4.5.10}$$

where Ω_0 is the volume of the primitive unit cell. The Born effective charge tensors are connected to the mixed second-order derivative of the energy with respect to atomic displacements and macroscopic electric field [7].

Finally, we discuss two phenomena that arise from the same basic mechanism: the coupling between the macroscopic electric field and the polarization associated with the $\mathbf{q} \rightarrow \mathbf{0}$ atomic displacements. The Born effective charges are involved in both cases.

First, in the computation of the low-frequency (infrared) dielectric permittivity tensor, one has to include the response of the ions. Their motion will be triggered by the force due to the electric field, while their polarization will be created by their displacement.

At the lowest order of approximation in the theory, the macroscopic frequency-dependent dielectric permittivity tensor $\epsilon_{\alpha\beta}(\omega)$ is calculated as follows:

$$\epsilon_{\alpha\beta}(\omega) = \epsilon^{\infty}_{\alpha\beta} + \frac{4\pi}{\Omega_0} \sum_{m} \frac{S_{m,\alpha\beta}}{\omega_m^2 - \omega^2}, \tag{4.5.11}$$

where the mode-oscillator strength $S_{m,\alpha\beta}$ is defined as:

$$S_{m,\alpha\beta} = \left(\sum_{\kappa\alpha'} Z^*_{\kappa,\alpha\alpha'} U^*_{m\mathbf{q}=\mathbf{0}}(\kappa\alpha') \right) \left(\sum_{\kappa'\beta'} Z^*_{\kappa',\beta\beta'} U_{m\mathbf{q}=\mathbf{0}}(\kappa'\beta') \right). \tag{4.5.12}$$

A damping factor might be added to equation (4.5.11) in order to take into account anharmonic effects, and fit frequency-dependent experimental data. For our purpose, such a damping factor can be ignored.

At zero frequency, the static dielectric permittivity tensor is usually denoted $\epsilon^0_{\alpha\beta}$; it is obtained by:

$$\epsilon^0_{\alpha\beta} = \epsilon^\infty_{\alpha\beta} + \sum_m \Delta\epsilon_{m,\alpha\beta} = \epsilon^\infty_{\alpha\beta} + \frac{4\pi}{\Omega_0} \sum_m \frac{S_{m,\alpha\beta}}{\omega_m^2}. \tag{4.5.13}$$

In parallel to this decomposition of the static dielectric tensor, one can define a mode-effective charge vector:

$$Z^*_{m,\alpha} = \frac{\sum_{\kappa\beta} Z^*_{\kappa,\alpha\beta} U_{m\mathbf{q}=\mathbf{0}}(\kappa\beta)}{\left(\sum_{\kappa\beta} U^*_{m\mathbf{q}=\mathbf{0}}(\kappa\beta) U_{m\mathbf{q}=\mathbf{0}}(\kappa\beta) \right)^{1/2}}. \tag{4.5.14}$$

This vector is related to the global polarization resulting from the atomic displacements for a given phonon mode m. The non-zero components indicate the directions in which the mode is infrared active.

Second, in the computation of phonons in the long-wavelength limit, a macroscopic polarization and electric field can be associated with the atomic displacements. At the simplest level of theory, the phonon eigenfrequencies then depend on the direction along which the limit is taken as well as on the polarization of the phonon. This gives birth to the LO–TO splitting, and to the Lyddane–Sachs–Teller relation [7].

For insulators, the non-analytical, direction-dependent part of the dynamical matrix $\tilde{C}^{\mathrm{NA}}_{\kappa\alpha,\kappa'\beta}(\mathbf{q} \to \mathbf{0})$ is given by:

$$\tilde{C}^{\mathrm{NA}}_{\kappa\alpha,\kappa'\beta}(\mathbf{q} \to \mathbf{0}) = \frac{4\pi}{\Omega_0} \frac{\left(\sum_\gamma q_\gamma Z^*_{\kappa,\gamma\alpha} \right) \left(\sum_{\gamma'} q_{\gamma'} Z^*_{\kappa',\gamma'\beta} \right)}{\sum_{\alpha\beta} q_\alpha \epsilon^\infty_{\alpha\beta} q_\beta}. \tag{4.5.15}$$

Hence, once the dynamical matrix at $\mathbf{q} = \mathbf{0}$ as well as $\epsilon^\infty_{\alpha\beta}$ and the Born effective charge tensors are available, it is possible to compute the LO–TO splitting of phonon frequencies at $\mathbf{q} = \mathbf{0}$.

Technical details

All our calculations are performed using the ABINIT package, developed by the authors and collaborators [8]. The exchange–correlation energy is evaluated within the local density approximation (LDA) to DFT, using the Perdew–Wang parametrization [9] of Ceperley–Alder electron-gas data [10].

Only valence electrons are explicitly considered using pseudopotentials to account for core–valence interactions. We use norm-conserving pseudopotentials [11, 12] with Hf(5s, 5p, 5d, 6s), Zr(4s, 4p, 4d, 5s), Si(3s, 3p) and O(2s, 2p) levels treated as valence states.

The wave functions are expanded in plane waves up to a kinetic energy cut-off of 30 Ha. The chosen kinetic energy cut-off and *k*-point sampling of the Brillouin zone ensure convergence of all the calculated properties.

Crystalline oxides

Introduction

Hafnia (HfO_2) and zirconia (ZrO_2) have many similar physical and chemical properties. These similarities result from the structural resemblance between the two oxides, which can in turn be explained by the chemical homology of Hf and Zr.

The electron configuration of hafnium is $4f^{14}5d^{2}6s^{2}$ while it is $4d^{2}5s^{2}$ for zirconium. In the periodic table, the inner transition (rare-earth) elements immediately preceding Hf add electrons to the inner 4f shell from element no 58, cerium, to no 71, lutetium. Because the nuclear charge increases while no additional outer shells are filled, there is a contraction in the atomic size. Consequently, element no 72, hafnium, has a slightly smaller atomic size than element no 40, zirconium, the group IVB element in the preceding. This results in the so-called lanthanide contraction. The atomic radii of Hf and Zr are close to each other: 1.44 and 1.45 Å, respectively [13]. They also have quasi-identical ionic radii (M^{4+}), 0.78 for Hf and 0.79 Å for Zr, respectively [14]. Their electronegativity values are almost equal, 1.23 for hafnium and 1.22 for zirconium [15]. All this explains the origin of the similarity between HfO_2 and ZrO_2.

Hafnia and zirconia undergo polymorphic transformations with changes in external parameters. At high temperature, the compounds are highly defective and their structure is fluorite type ($Fm\overline{3}m$). The decreasing temperature induces a cubic to tetragonal ($P4_2/nmc$) phase transition (c–t) at about 2650°C for HfO_2 [16] and about 2350°C for ZrO_2 [17]. This transition is followed by a tetragonal to monoclinic ($P2_1/c$) martensitic phase transition (t–m) at about 1650°C for hafnia [18] and about 1150°C for zirconia [19].

The crystalline structure may also depend on the presence of dopants (MgO, CaO, Y_2O_3). For instance, an addition of 3% (wt) Y_2O_3 stabilizes the tetragonal form of ZrO_2 at room temperature [20]. Finally, the contribution of the surface energy also influences the structural stability of nanocrystallites. A crystallite of 30 nm or less is now believed to stabilize the tetragonal form of ZrO_2 at room temperature [21], while for HfO_2 the critical size is about 10 nm [22].

The structural, electronic and dynamical properties of hafnia and zirconia have been the object of several first-principles studies [23–27]. For the sake of brevity, our results are only presented here for the cubic and tetragonal phases. For the monoclinic phase, we refer the interested reader to the work of Zhao and Vanderbilt [26, 27].

Structural properties

The cubic and tetragonal crystalline structures of HfO_2 and ZrO_2 are illustrated in figure 4.5.1. The cubic phase takes the fluorite structure (space group $Fm\overline{3}m$), which is fully characterized by a single lattice constant a. The M = (Hf, Zr) atoms are in a face-centred-cubic structure and the O atoms occupy the tetrahedral interstitial sites associated with this fcc lattice. The unit cell contains one formula unit of MO_2 with M = (Hf, Zr). The tetragonal phase (space group $P4_2/nmc$) can be viewed as a distortion of the cubic structure obtained by displacing alternating pairs of O atoms up and down by an amount Δz along the z direction, as shown in figure 4.5.1, and by applying a tetragonal strain. The resulting primitive cell is doubled compared to the cubic phase, including two formula units of MO_2. The tetragonal structure is completely specified by two lattice constants (a and c) and the dimensionless ratio $d_z = \Delta z/c$ describing the displacement of the O atoms. The cubic phase can be considered as a special case of the tetragonal structure with $d_z = 0$ and $c/a = 1$ (if the primitive cell is used for the tetragonal phase, $c/a = \sqrt{2}$).

In table 4.5.1, our calculated structural parameters for the cubic and tetragonal phases of HfO_2 and ZrO_2 are compared with the experimental

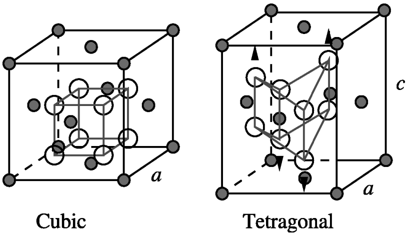

Figure 4.5.1. Structures of the cubic and tetragonal phases of HfO_2 and ZrO_2. The O atoms are in white while M = (Hf, Zr) atoms are in grey. For clarity, the Zr–O bonds are not indicated. For the tetragonal phase, the arrows indicate the displacements of oxygen pairs relative to the cubic structure.

Table 4.5.1. Structural parameters for the cubic (C) and tetragonal (T) phases of HfO_2 and ZrO_2.

	HfO_2		ZrO_2	
	Theoretical	Experimental	Theoretical	Experimental
C				
a	5.11	5.08	5.01	5.09
Volume	33.36	32.77	31.44	32.97
d(M–O)	2.21	2.20	2.17	2.20
T				
a	5.11	5.15	5.02	5.05
c	5.17	5.29	5.09	5.18
d_z	0.0310	–	0.0400	0.0574
Volume	33.75	35.08	32.07	33.04
d(M–O)	2.13	–	2.07	2.05
	2.32	–	2.31	2.39

The length unit is the Å. The experimental results for HfO_2 are taken from [28], while those for ZrO_2 are obtained by extrapolation to zero temperature using the thermal expansion data of Aldebert and Traverse [19].

values [19, 28]. The agreement is very good: the errors on the lattice constants and the volumes are smaller than 2%, as is typical for LDA calculations. The largest discrepancy is for d_z in *t*-ZrO_2 (the small displacement from the cubic phase localization): our value is about 30% smaller than the experimental data, but it is in excellent agreement with the results of other first-principles calculations. The discrepancy with experiment is probably due to the fact that our calculations are performed at zero temperature.

The bond lengths are also found to be in good agreement with experimental data, as indicated in table 4.5.1. In both the cubic and tetragonal structures, the M = (Hf, Zr) atoms are eightfold coordinated and the O atoms are fourfold coordinated. However, in the tetragonal phase, four O atoms are closer to the M = (Hf, Zr) atom than the other four (8 and 10% difference in the Hf–O and Zr–O bond lengths, respectively).

Born effective charge tensors

In table 4.5.2, we report non-vanishing components of the calculated Born effective charge tensors for M = Hf, Zr) and O atoms in the cubic and tetragonal phases of hafnia and zirconia. Due to the symmetry of the cubic phase, the Born effective charge tensors of M = (Hf, Zr) and O atoms are diagonal and isotropic. The value of Z^* is anomalously large for M = (Hf, Zr)

Table 4.5.2. Non-vanishing components of the calculated Born effective charge tensors for M = (Hf, Zr) and O atoms in the cubic (C) and tetragonal (T) phases of HfO_2 and ZrO_2.

Atom	HfO_2	ZrO_2
C		
M	(+5.58 +5.58 +5.58)	(+5.74 +5.74 +5.74)
O	(−2.79 −2.79 −2.79)	(−2.87 −2.87 −2.87)
T		
M	(+5.57 +5.57 +5.24)	(+5.74 +5.74 +5.14)
O	(−3.22 −2.35 −2.62)	(−3.51 −2.24 −2.57)

The tensors are diagonal and only the principal elements are given.

atoms compared to the nominal ionic charge $Z = 4$. This behaviour has also been observed in the case of $PbZrO_3$ [29], and indicates a mixed covalent–ionic bonding. In the tetragonal structure, the symmetry imposes that the Born effective charge tensor of M = (Hf, Zr) atoms is diagonal and only has two independent components: parallel ($Z^*_{||}$) and perpendicular ($Z^*_{\perp}$) to the *c*-axis. The value of $Z^*_{\perp}$ is identical to the one calculated for the cubic phase, while $Z^*_{||}$ is 6 and 10% smaller for HfO_2 and ZrO_2, respectively. The Born effective charge tensor of O atoms is also diagonal, but with three independent components. It is quite anisotropic compared to the cubic phase. Such a strong anisotropy of the Born effective charge tensor for O atoms has already been observed in SiO_2-stishovite [30] and TiO_2-rutile [31].

It is interesting to note that the Born effective charges of *c*-HfO_2 are about 3% smaller (in absolute value) than those of *c*-ZrO_2. The comparison between the Z^*-values of *t*-HfO_2 and *t*-ZrO_2 is also very instructive. In directions perpendicular to the *c*-axis, the Born effective charges of the M = (Hf, Zr) atoms compare in the same way as for the cubic phase, while the comparison for the Born effective charges of O atoms shows an anisotropy in *t*-ZrO_2 stronger than that in *t*-HfO_2 by about 30% (the values of $Z^*_{\perp}$ for *t*-HfO_2 are comprised between those of *t*-ZrO_2). In the direction parallel to the *c*-axis, the Born effective charges in *t*-HfO_2 are larger than in *t*-ZrO_2 by about 2%, showing an opposite trend with respect to the comparison for the cubic phase. The slightly different behaviour between hafnia and zirconia can be related to the differences in the inner electronic shells between Hf and Zr, which lead to different polarizabilities. This discussion shows the interest of analysing a dynamical property such as the Born effective charge tensors, which is able to highlight subtle differences between two very similar systems.

Phonon frequencies at the Γ point

The theoretical group analysis predicts the following irreducible representations of optical and acoustical zone-centre modes for the cubic phase:

$$\Gamma = \underbrace{F_{2g}}_{\text{Raman}} \oplus \underbrace{F_{1u}}_{\text{IR}} \oplus \underbrace{F_{1u}}_{\text{Acoustic}}$$

and for the tetragonal phase:

$$\Gamma = \underbrace{A_{1g} \oplus 2B_{1g} \oplus 3E_g}_{\text{Raman}} \oplus \underbrace{A_{2u} \oplus 2E_u}_{\text{IR}} \oplus \underbrace{A_{2u} \oplus E_u}_{\text{Acoustic}} \oplus \underbrace{B_{2u}}_{\text{Silent}} .$$

Because of the non-vanishing components of the Born effective charge tensors, the dipole–dipole interaction must be properly included in the calculation of the interatomic force constants [7, 32, 33]. In particular, the dipole–dipole contribution is found to be responsible for the splitting at the Γ point between the longitudinal and transverse optic (LO and TO, respectively) modes F_{1u} in the cubic phase, and E_u (perpendicular to the c-axis) and A_{2u} (parallel to c-axis) in the tetragonal phase.

In the absence of experimental data for the cubic phase of both materials and for the tetragonal phase of hafnia, the following discussion will first focus on the tetragonal phase of zirconia. A comparison will then be made between the calculated results for the various phases of both materials.

In the experimental Raman spectra, six lines corresponding to the six active modes have been observed for pure t-ZrO_2 at high temperature [34, 35] and for samples stabilized by dopants [34, 36–38]. In the case of pure t-ZrO_2, the Raman spectra are found to be very similar except for a slight down-shift of the frequencies, which was attributed to the increase in lattice constant with dopant concentration and to temperature effects [34]. In the absence of t-ZrO_2 single crystals of good quality, a reliable assignment of those lines could not be made. However, the symmetry classification proposed by Feinberg and Perry [34] is widely used in the literature. It is reported in table 4.5.3, together with the measured phonon frequencies for their yttria-stabilized t-ZrO_2 sample. Theoretical studies have been performed using lattice-dynamical models, and phonon frequencies in relatively good agreement with the experimental values have been predicted [39–41]. Consequently, the symmetry assignments given by Feinberg and Perry [34] were criticized and a second set of assignments was proposed. In particular, Mirgorodsky *et al* [40, 41] argued that the A_{1g} mode should be at lower frequency to account for the change in the dynamical properties of ZrO_2. More recently, using crystallite size effects to stabilize the tetragonal phase, Bouvier and Lucazeau [42] obtained experimental Raman spectra of pure t-ZrO_2 at room temperature. They proposed a third assignment of the vibration modes on the basis of a linear chain model: compared to Feinberg

Table 4.5.3. Fundamental frequencies of the cubic (C) and tetragonal (T) phases of HfO_2 and ZrO_2 (in cm^{-1}) with their symmetry assignments.

	HfO_2	ZrO_2		
Mode	Theoretical	Theoretical	Experimental	
C				
Raman				
F_{2g}	579	596		
Infrared				
F_{1u} (TO)	285	280		
F_{1u} (LO)	630	677		
T				
Raman				
A_{1g}	218	259	266 (E_g)	269 (E_g)
$B_{1g}(1)$	244	331	326	319
$B_{1g}(2)$	582	607	616 (A_{1g})	602 (A_{1g})
$E_g(1)$	110	147	155 (B_{1g})	149
$E_g(2)$	479	474	474	461
$E_g(3)$	640	659	645	648 (B_{1g})
Infrared				
A_{2u} (TO)	315	339	320	339
A_{2u} (LO)	621	664	–	650 (E_u)
E_u (TO1)	185	153	140	164
E_u (LO1)	292	271	–	232
E_u (TO2)	428	449	550	467
E_u (LO2)	669	734	–	734 (m-ZrO_2)
Silent				
B_{2u}	665	673		

For tetragonal zirconia, the experimental values of the Raman modes are taken from [34, 42] (in the last two columns, respectively). For the infrared modes, the data for t-ZrO_2 are from [37, 39] (in the last two columns, respectively).

and Perry [34], it consists in an interchange of the B_{1g} mode and the highest E_g mode (see table 4.5.3).

As for the infrared (IR) spectra of t-ZrO_2, experiments have been carried out on crystals [43], doped powders [34, 37, 44] and undoped powders stabilized by their small particle size [39]. But, in the absence of t-ZrO_2 single crystals of good quality, a general agreement has not been reached so far. The two most recent studies [37, 39], which are reported in table 4.5.3, agree to assign the E_u TO modes to the lines at about 150 and 500 cm^{-1}. These assignments were also confirmed by calculations [39–41]. However, the situation is more confused for the A_{2u} mode. To properly fit their reflectance spectra, Pecharromán *et al* [39] had to introduce three oscillators in addition to the two E_u modes. They placed the A_{2u} at 339 cm^{-1} and attributed the extra modes at 580 and 672 cm^{-1} to a secondary oscillator and to the presence of monoclinic zirconia, respectively. Hirata *et al* [37] also mentioned a broad band located at 320 cm^{-1}, but they attributed it to a B_u mode associated with traces of monoclinic zirconia.

Our calculated phonon frequencies and symmetry assignments are reported in table 4.5.3, where they are compared with those of various experimental results for t-ZrO$_2$. For the phonon frequencies, our results are globally in better agreement with experimental data than those of previous theoretical studies. Our symmetry assignments meet all the requirements discussed in the literature, solving the existing contradictions and clarifying some important issues.

For the Raman spectra of t-ZrO$_2$, our calculation presents an rms absolute deviation of 8.4–9.6 cm^{-1}, and an rms relative deviation of 2.7–2.6% with respect to the experimental data of Feinberg and Perry [34] and those of Bouvier and Lucazeau [42]. Our symmetry assignments reconcile the arguments developed by Mirgorodsky *et al* [40, 41] with those proposed by Bouvier and Lucazeau [42]. On the one hand, the A_{1g} mode is at lower frequency compared to the assignments by Feinberg and Perry, in agreement with the arguments of Mirgorodsky *et al* [40, 41]. On the other hand, the B_{1g} is found to have high frequency in accordance with Bouvier and Lucazeau [42].

For the IR-active frequencies of t-ZrO$_2$, our calculation presents an rms absolute deviation of 18.8 and 59.5 cm^{-1}, and an rms relative deviation of 7.6 and 12.3%, with respect to the experimental data of Pecharromán *et al* [39] and Hirata *et al* [37], respectively. We find an LO–TO splitting for the A_{2u} mode of 325 cm^{-1}, much larger than the 15 cm^{-1} found by Pecharromán *et al* [39]. Our result is consistent with the large difference between ϵ_∞ and ϵ_0 as discussed in the 'Dielectric permittivity tensors' section. As a result, we propose that the LO peaks at 650 and 734 cm^{-1} should be attributed to the A_{2u} and the second E_u modes.

In table 4.5.4, we indicate the relationship between the phonon modes of the cubic and tetragonal phases in the case of zirconia. Cubic zone boundary (X point) modes become zone-centre (Γ point) modes in the tetragonal structure. Note in particular that the unstable X_2^- zone-boundary mode in the cubic phase transforms into a stable zone-centre A_{1g} phonon in the tetragonal form.

It is also very interesting to compare the phonon frequencies calculated for HfO$_2$ and ZrO$_2$ (see table 4.5.3). There are several possible origins for the variations that are observed: structural changes (e.g. the volume), change of the mass ratio Hf/Zr $= 1.96$, and differences in interatomic force constants. Given the small structural changes reported in table 4.5.1, we suspect that their effect should be very small. In order to check this, we compute the

Table 4.5.4. Relationship of phonon modes for cubic and tetragonal phases.

	Cubic					Tetragonal	
	Γ		X			Γ	
Acoustic	F_{1u}	0			→	A_{2u}	0
					→	E_u	0
			X_4^-	361	→	B_{1g}	331
			X_5^-	141	→	E_g	147
Optic	F_{2g}	596			→	B_{1g}	607
					→	E_g	659
			X_2^-	191i	→	A_{1g}	259
			X_5^-	568	→	E_g	474
	F_{1u}	280			→	A_{2u}	339
					→	E_u	153
			X_1^+	697	→	B_{2u}	673
			X_5^+	325	→	E_u	449

The calculated frequencies are given in cm^{-1}. For the infrared modes, only the TO frequencies are reported.

phonon frequencies for hafnia assuming that the interatomic force constants are the same as those for zirconia, while the volume is allowed to vary. This analysis shows that the structural changes play a very minor role, in agreement with our intuition. As for the role of the mass ratio, it can be clearly evidenced in the modes in which the M = (Hf, Zr) atoms move significantly more than O atoms: the $B_{1g}(1)$ and $E_g(1)$ modes of the tetragonal phase for which the frequencies vary by about 35%. In contrast, the modes in which the M = (Hf, Zr) atoms are not involved (i.e. F_{2g} in the cubic phase, and A_{1g} and B_{2u} in the tetragonal phase), as well as those for which the O atoms move significantly more than the M = (Hf, Zr) atoms (i.e. F_{1u} in the cubic phase, and $B_{1g}(2)$, $E_g(2)$ and (3), A_{2u}, and $E_u(1)$ and (2) in the tetragonal phase), should have frequencies very similar in HfO_2 and ZrO_2. This is indeed what is observed in most of the cases. However, there are some significant exceptions for the tetragonal phase: A_{1g} and $E_u(1)$ for which the frequencies vary by 19 and 17%, respectively. These are cases in which the effects due to differences in the interatomic force constants are dominant.

Dielectric permittivity tensors

In the cubic phase, the electronic (ϵ_∞) and static (ϵ_0) permittivity tensors are diagonal and isotropic. Due to the symmetry of the tetragonal crystal, these tensors are still diagonal, but have two independent components $\epsilon_\parallel$ and $\epsilon_\perp$, parallel and perpendicular to the c-axis, respectively. In table 4.5.5, the

Table 4.5.5. Electronic and static dielectric tensors for the cubic (C) and tetragonal (T) phases of HfO_2 and ZrO_2.

	HfO_2		ZrO_2	
C				
ϵ_∞	5.37		5.74	
$\Delta\epsilon$	20.80		27.87	
ϵ_0	26.17		33.61	
T				
	$\|$	$\perp$	$\|$	$\perp$
ϵ_∞	5.13	5.39	5.28	5.74
$\Delta\epsilon_1$	14.87	22.34	15.03	35.48
$\Delta\epsilon_2$		5.08		6.91
ϵ_0	20.00	32.81	20.31	48.13

The contributions of the different phonon modes to the static dielectric tensor are also indicated. For the cubic phase, the tensors are diagonal and isotropic. The phonon mode contributions to $\epsilon_0^{\|}$ come from the IR-active F_{1u} mode. For the tetragonal phase, the tensors are also diagonal but they have different components parallel ($\|$) and perpendicular ($\perp$) to the c-axis. The phonon mode contributions to $\epsilon_0^{\|}$ come from the IR-active A_{2u} mode, while the contributions to $\epsilon_0^{\perp}$ come from the two IR-active E_u modes.

calculated values of ϵ_∞ and ϵ_0 are reported for the cubic and the tetragonal phases of hafnia and zirconia. In the tetragonal phase, the ϵ_∞ tensor is only slightly anisotropic with about 5 and 10% difference between the parallel and perpendicular values for t-HfO_2 and t-ZrO_2, respectively. In contrast, the ϵ_0 tensor is highly anisotropic: the value of ϵ_0 in the direction parallel to the c-axis is 1.6 and 2.4 times smaller than that in the perpendicular direction for t-HfO_2 and t-ZrO_2, respectively. While the values of ϵ_∞ for the cubic and tetragonal phases are very close, there is a significant difference in the values of ϵ_0.

A direct comparison of the calculated dielectric tensors with experimental values is very difficult since there are very few data available in the literature, especially for hafnia. The main problem encountered in the experimental determination of the dielectric properties is that good quality single crystals are not available. For the tetragonal phase, the results obtained for undoped powders stabilized by their small particle size must be analysed in the framework of effective medium theory [45]. As a result, a unique value of ϵ is found without distinction between the directions parallel and perpendicular to the c-axis. In order to compare our results with experimental data, we average the values parallel and perpendicular to the c-axis:

$$\bar{\epsilon} = \frac{2\epsilon_\perp + \epsilon_\|}{3}.$$

This average does not really have any physical meaning, and therefore the comparison is rather qualitative.

For hafnia, we are only aware of measurements of ϵ_0. Our calculated values of 26.17 for the cubic phase, and $\bar{\epsilon}_0 = 28.54$ for the tetragonal phase significantly overestimate the values of 16 [46] and 20 [47] obtained in recent measurements. This overestimation is considerably higher than what can be expected from our density functional approach and the origin of this difference remains poorly understood. For the cubic phase, our results agree within 1% with those obtained by Zhao and Vanderbilt [26] using similar methods. However, for the tetragonal phase, our calculations disagree significantly with those of Zhao and Vanderbilt [26]. In fact, we find a ratio of 1.6 between the values of the ϵ_0 tensor in directions parallel and perpendicular to the c-axis, to be compared with the value of 8.6 reported by Zhao and Vanderbilt [26]. We note that the value of $\bar{\epsilon}_0 = 70$ proposed by the latter authors appears excessively high in view of the dielectric constant of the cubic phase ($\sim$26.17) and the trends observed for zirconia (see below).

For zirconia, an experimental value of $\epsilon_\infty = 4.8$ is reported in the literature for c-ZrO$_2$ [43, 48], while measured values for t-ZrO$_2$ range between 4.2 [39] and 4.9 [49]. Our theoretical values ($\epsilon_\infty = 5.74$ and $\bar{\epsilon}_\infty = 5.59$ for the cubic and tetragonal phases, respectively) are larger than the experimental ones by about 10–15%, as often found in the LDA to DFT. For ϵ_0, the experimental values found in the literature vary from 27.2 [50] to 29.3 [51] for c-ZrO$_2$, and from 34.5 [51] to 39.8 [51] for t-ZrO$_2$. For the cubic phase, our calculated value $\epsilon_0 = 33.61$ is somewhat larger than experimental estimates, whereas, for the tetragonal phase, our calculated average $\bar{\epsilon}_0 = 38.86$ falls in the range of the experimental data.

For a deeper analysis of the static dielectric tensor, we can rely not only on the frequencies of the IR-active modes, but also on the corresponding eigendisplacements and Born effective charges. Indeed, the static dielectric tensor can be decomposed in the contributions of different modes as indicated in equation (4.5.13).

The contribution of the individual modes $\Delta\epsilon_m$ to the static dielectric constants is presented in table 4.5.5. For each IR-active mode, the relevant component of the oscillator strength tensor is reported in table 4.5.6. This tensor is isotropic for the F_{1u} mode in the cubic phase, while in the tetragonal phase we indicate the parallel–parallel component for the A_{2u} mode, and the perpendicular–perpendicular component for the E_u modes. We also give the magnitude of the mode-effective charge vector defined by equation (4.5.14) which is parallel and perpendicular to the tetragonal axis for A_{2u} and E_u modes, respectively, while it has an arbitrary orientation for the F_{1u} mode. The atomic motions for these vibrational modes have been described in detail in the literature [39, 52, 53].

In table 4.5.6, the $E_u(1)$ mode in the tetragonal phase has the lowest oscillator strength (S_m) and the lowest mode-effective charge (Z^*_m). However, it also has the lowest frequency (see table 4.5.3), which results in the largest contribution to the static dielectric constant in table 4.5.5. The F_{1u} mode in the cubic phase has similar characteristics: the oscillator strength is quite small (though larger than for the $E_u(1)$ mode) but it also has a low frequency (though not as low as for the $E_u(1)$ mode). The resulting contribution is of the same order of magnitude as the $E_u(1)$ mode in the tetragonal phase (though rather smaller). Comparatively, the $E_u(2)$ mode in the tetragonal phase gives a much smaller (but not negligible) contribution despite its larger oscillator strength and mode-effective charge.

In fact, the frequency factor plays a crucial role in equation (4.5.13). The A_{2u} has the largest oscillator strength (about twice that of the $E_u(1)$ mode) and the largest mode-effective charge. However, its frequency is about twice that of the $E_u(1)$ mode, and its contribution to the static dielectric constant is roughly half that of the $E_u(1)$ mode. This difference between A_{2u} and E_u modes explains why the ϵ_0 tensor is highly anisotropic, while the ϵ_∞ tensor is only slightly anisotropic.

The same argument holds to rationalize the differences observed in the static dielectric tensor between the tetragonal and the cubic phases. Indeed, as already mentioned, the oscillator strength and the mode-effective charge of the F_{1u} mode are comparable to those of the E_u modes of the tetragonal phase, while the frequency of the F_u mode is 1.7 times larger than that of the $E_u(1)$ mode. As a result, the static dielectric constant is noticeably smaller in the cubic case.

In table 4.5.6, it can be observed that the oscillator strengths and the mode-effective charges are smaller for HfO_2 than for ZrO_2. This can be

Table 4.5.6. Components of mode-effective charge vectors Z_m^* and oscillator strength tensor S_m for each of the IR-active modes of the cubic (C) and tetragonal (T) phases of HfO_2 and ZrO_2.

	HfO_2		ZrO_2	
	Z_m^*	S_m	Z_m^*	S_m
C				
F_{1u}	5.82	6.31	6.42	7.65
T				
A_{2u}	7.71	11.10	8.14	12.28
$E_u(1)$	5.75	5.76	5.95	5.91
$E_u(2)$	5.91	7.03	6.99	9.95

The description of the reported vector and tensor components corresponding to the different modes is given in the text. The components of the mode-effective charge vectors are given in units of $|e|$, where e is the electronic charge. The oscillator strengths are given in 10^{-4} atomic units (1 a.u. = 0.342 036 m^3 s^{-2}).

related to the behaviour of the Born effective charges $Z^{*}_{\kappa,\alpha\alpha'}$ and the eigendisplacements $U_m(\kappa\alpha)$, the two quantities that appear in the definitions of $S_{m,\alpha\beta}$ and $Z^{*}_{m,\alpha}$ given in equations (4.5.12) and (4.5.14). On the one hand, as discussed in the 'Born effective charge tensors' section, the Born effective charges are globally smaller in HfO_2 than in ZrO_2. On the other hand, the displacements of Hf atoms are smaller than those of Zr atoms simply because they are heavier (as discussed in the 'Phonon frequencies at the Γ point' section).

If one now considers the contributions to the static dielectric constant reported in table 4.5.5, it appears clearly that for HfO_2 the contributions are smaller than for ZrO_2. However, despite the fact that in all cases the oscillator strengths are smaller for hafnia than for zirconia, two different situations can be distinguished depending on the behaviour of the phonon frequencies. On one hand, for the $E_u(1)$ mode, the frequency for HfO_2 is larger than for ZrO_2. In this case, the contribution for ZrO_2 is noticeably larger (about 60%) than for HfO_2. For the F_{1u} in the cubic phase, the situation is very similar though the frequency does not change very much. On the other hand, for the A_{2u} mode, the frequency changes in the opposite way. As a result, the increase by 6% of the oscillator strengths is almost completely compensated by the rise of 7% in the frequency: in the end, there only remains a 1% difference between the contributions for HfO_2 and ZrO_2. For the $E_u(2)$ mode, the rise of 5% in the frequency only slightly attenuates the 15% increase of the oscillator strengths.

Crystalline silicates

Introduction

Due to the chemical homology of Hf and Zr discussed in the 'Introduction' section, hafnon ($HfSiO_4$) and zircon ($ZrSiO_4$) resemble each other in many physical and chemical properties. Their similarities are such that there is complete miscibility between $ZrSiO_4$ and $HfSiO_4$ [54]. In addition to their importance as potential alternative gate dielectrics, hafnon and zircon are of geological significance. They both belong to the orthosilicate class of minerals, which can be found in igneous rocks and sediments. Zircon is used as a gemstone, because of its good optical quality, and resistance to chemical attack. In the earth's crust, hafnon and zircon are host minerals for the radioactive elements uranium and thorium. Therefore, they have been widely studied in the framework of nuclear waste storage.

In a recent paper [55], we have studied the structural, electronic and dynamical properties of zircon using first-principles calculations. In this section, we present a comparison between hafnon and zircon.

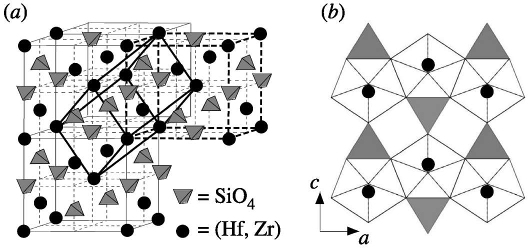

Figure 4.5.2. Structure of hafnon and zircon. (*a*) The individual SiO$_4$ units are represented schematically by the grey tetrahedra, while M = (Hf, Zr) atoms are indicated by black spheres. The two sets of dashed lines and heavy lines outline the body-centred-tetragonal unit cell and the primitive cell, respectively. (*b*) Besides the SiO$_4$ units, the MO$_8$ triangular dodecahedra with the M atoms in their centre are also drawn.

Structural properties

Hafnon and zircon have a conventional unit cell which is body-centred tetragonal (space group $I4_1/amd$, no 141) and contains four formula units of MSiO$_4$ with M = (Hf, Zr), as illustrated by the dashed lines in figure 4.5.2(*a*). A primitive cell containing only two formula units of MSiO$_4$ can also be defined, as indicated by the heavy lines in figure 4.5.2(*a*).

The structure of hafnon and zircon may be viewed as consisting of $(\mathrm{SiO_4})^{4-}$ anions and M^{4+} cations with M = (Hf, Zr), as illustrated by the grey tetrahedra and the black spheres in figure 4.5.2(*a*). This is consistent with the larger bond length (about 25%) of the M–O compared to the Si–O bond. The experimental data describing the structure of hafnon [54] and zircon [56] are reported in table 4.5.7.

Alternatively, as presented in figure 4.5.2(*b*), a different view may be adopted in which HfSiO$_4$ and ZrSiO$_4$ consist of alternating (discrete) SiO$_4$ tetrahedra and MO$_8$ units, sharing edges to form chains parallel to the *c*-direction. Note that in these MO$_8$ units four O atoms are closer to the M atom than the other four (about 6% difference in the M–O bond length; see table 4.5.7).

The positions of the M = (Hf, Zr) and Si atoms are imposed by symmetry: they are located at $(0, \frac{3}{4}, \frac{1}{8})$ and $(0, \frac{1}{4}, \frac{3}{8})$ on the 4a and 4b Wyckoff sites, respectively. The O atoms occupy the 16h Wyckoff sites $(0, u, v)$, where u and v are internal parameters.

Table 4.5.7 summarizes our results obtained after structural and atomic relaxation. The calculated lattice constants a and c, as well as the internal parameters u and v, are found to be in excellent agreement with their corresponding experimental values [54, 56]. Interatomic distances and angles are within 1 or 2% of the experimental values. This accuracy is to address in a meaningful way the dynamical and dielectric properties.

Table 4.5.7. Structural parameters of $HfSiO_4$ and $ZrSiO_4$.

	$HfSiO_4$		$ZrSiO_4$	
	Theoretical	Experimental	Theoretical	Experimental
a	6.61	6.57	6.54	6.61
c	5.97	5.96	5.92	6.00
u	0.0672	0.0655	0.0645	0.0646
v	0.1964	0.1948	0.1945	0.1967
Volume	130.42	128.63	126.60	131.08
d(Si–O)	1.62	1.61	1.61	1.62
d(M–O)	2.14	2.10	2.10	2.13
	2.27	2.24	2.24	2.27
∠(O–Si–O)	97°	97°	97°	97°
	116°	117°	116°	116°

The length unit is the Å. The experimental data are taken from [54] for $HfSiO_4$, and from [56] for $ZrSiO_4$.

Electronic structure

In figure 4.5.3, we present the calculated electronic density of states (DOS) for hafnon and zircon. The complete electronic band structure for $ZrSiO_4$ along several directions in the Brillouin zone can be found elsewhere [55]. For $HfSiO_4$, the electronic band structure is very similar apart from the position of the Hf 5s and 5p bands, as explained hereafter.

We clearly distinguish four groups in the DOS of the valence bands, of which the three lowest ones are rather peaked (small dispersion of the bands), indicative of a weak hybridization. The DOS of hafnon (zircon) exhibits a very sharp peak at -60.2 eV (-47.1 eV) attributed to the Hf 5s (Zr 4s) states, corresponding to two flat bands in the band structure [55]. The peak at -29.8 eV for hafnon (-25.5 eV for zircon) is related to the Hf 5p (Zr 4p) states: it includes six electrons per unit cell. The O 2s peak (eight electrons per unit cell) is located between -18.0 and -16 eV for both hafnon and zircon.

By contrast, the fourth group (24 electrons per unit cell) has a much wider spread of 8 eV. These states have mainly an O 2p character with some mixing of Si and M = (Hf, Zr) orbitals. This mixed covalent–ionic bonding of $HfSiO_4$ and $ZrSiO_4$, appearing in this group of valence bands, should be kept in mind when interpreting the Born effective charge tensors.

Born effective charge tensors

In the hafnon and zircon structures, the local site symmetry of M = (Hf, Zr) and Si atoms is rather high ($\bar{4}m2$). The Born effective charge tensors of

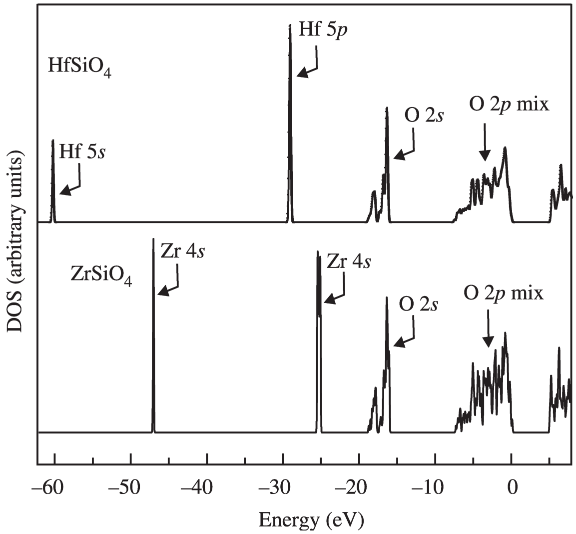

Figure 4.5.3. Electronic DOS for $HfSiO_4$ and $ZrSiO_4$.

M = (Hf, Zr) and Si atoms are diagonal and have only two independent components: parallel and perpendicular to the tetragonal axis, $Z^*_\parallel$ and $Z^*_\perp$, respectively. The Born effective charge tensors of M = (Hf, Zr) and Si atoms are reported in table 4.5.8.

We note that $Z^*_\perp$ for M = (Hf, Zr) is anomalously large compared to the nominal ionic charge of the hafnium and zirconium ions $Z = +4$. A similar behaviour was also observed in the case of $PbZrO_3$ [29] and of hafnia and zirconia, as discussed in 'Crystalline oxides' section. A detailed analysis of the physics of Born effective charges in the case of perovskite ferroelectrics (like $PbZrO_3$) ascribed this effect to a mixed covalent–ionic bonding [57]. In the 'Electronic structure' section, we have seen the occurrence of M–O 2p hybridization. Thus, the physical interpretation of this phenomenon is probably similar to the case of perovskite ferroelectrics. The other component of the M = (Hf, Zr) Born effective charge tensor ($Z^*_\parallel$) is also larger than the nominal ionic charge, although the effect is not as pronounced.

For the silicon atom, there are also some (weaker) deviations with respect to the nominal value ($Z = +4$), one component being slightly larger, and one being definitely lower. These are not very different from those observed in tetrahedrally bonded silica polymorphs, like quartz [58], in which each O atom is strongly bonded to two Si atoms, or in the more compact polymorph of silica, stishovite [30], in which each O atom has three close Si neighbours.

Note that $Z^*_\perp$ is about 3% smaller for hafnium in $HfSiO_4$ than for zirconium in $ZrSiO_4$, similarly to what is observed in hafnia and zirconia,

Table 4.5.8. Non-vanishing components of the calculated Born effective charge tensors for M = (Hf, Zr), Si and O atoms in $HfSiO_4$ and $ZrSiO_4$.

Atom	$HfSiO_4$	$ZrSiO_4$
M	(+5.28 +5.28 +4.68)	(+5.41 +5.41 +4.63)
Si	(+3.18 +3.18 +4.35)	(+3.25 +3.25 +4.42)
O	$\begin{pmatrix} -1.15 & 0 & 0 \\ 0 & -3.08 & -0.19 \\ 0 & -0.35 & -2.26 \end{pmatrix}$	$\begin{pmatrix} -1.15 & 0 & 0 \\ 0 & -3.17 & -0.16 \\ 0 & -0.34 & -2.25 \end{pmatrix}$
	[−1.15 −3.16 −2.18]	[− 1.15 − 3.23 −2.19]

For M = (Hf, Zr) and Si atoms, the tensors are diagonal and only the principal elements are given. For O atoms, the full tensor is reported and the principal elements of its symmetric part are indicated between brackets.

as discussed in the 'Born effective charge tensors' section. The Born effective charge of Si atoms for directions perpendicular to the tetragonal axis shows a very similar behaviour: it is about 2% smaller in hafnon than in zircon. For the Born effective charge in a direction parallel to the *c*-axis, we find for Si atoms the same trend as for perpendicular directions, but the opposite one for M = (Hf, Zr) atoms, the Born effective charges for Hf in hafnon being about 1% higher than for Zr in zircon.

The local site symmetry of the O atoms has only a mirror plane. As a consequence, the Born effective charge tensors of O atoms are not diagonal, and depend on five independent quantities. We examine the tensor for the O atom located at (0, u, v), which is reported in table 4.5.8. The Born effective charge tensors of the other oxygen atoms can be obtained using the symmetry operations. For this particular atom, the mirror plane is perpendicular to x. Note that Z^*_{yz} and Z^*_{zy} are different, but rather small, making the Born effective charge tensor almost diagonal. They appear in the mirror plane, where one O–Si bond and two O–M bonds (one long and one short) are present. One can compute the projection of the Born effective charge on these directions: for the O–Si bond, the projection is −2.30 in $HfSiO_4$ (−2.29 in $ZrSiO_4$, while it is −3.16 (−3.23) for the shorter O–Hf (O–Zr) bond, and −2.97 (−3.02) for the longer bond. In this plane, the magnitude of the Born effective charge components is larger than the nominal ionic charge of oxygen ($Z = -2$). Following an alternative approach to the characterization of the anisotropy of this tensor, we select its symmetric part and diagonalize it. The principal values are given in table 4.5.8 and the principal direction associated with the largest principal value forms an angle of about 14° with the y-axis. Both analyses give the same type of anisotropy.

Such a strong anisotropy of the Born effective charge tensor for O atoms, with one component of magnitude much smaller than two and much smaller than the two others, has already been observed in SiO_2-stishovite [30] and TiO_2-rutile [31]. By contrast, in tetrahedrally bonded silica, there are *two* components of magnitudes much smaller than two. Thus, at the level of the Born effective charges, the ionic–covalent bonding of O atoms to M = (Hf, Zr) and Si atoms in $HfSiO_4$ and $ZrSiO_4$ is closer to stishovite than to quartz, in agreement with a naive bond-counting argument. Models of amorphous silicates MSi_xO_y should take into account this difference, and might be classified according to the anisotropy of the O Born effective charges. One expects that for a small content of M = (Hf, Zr) the quartzlike behaviour dominates, while for M atomic fractions closer to that of hafnon and zircon the stishovite-like behaviour becomes stronger.

Note finally that the Born effective charges for O atoms are very similar in $HfSiO_4$ and $ZrSiO_4$. The only significant difference is for the second principal value, which is 2% smaller in hafnon than in zircon.

Phonon frequencies at the Γ point

We also compute the phonon frequencies at the Γ point of the Brillouin zone for hafnon and zircon. The theoretical group analysis predicts the following irreducible representations of optical and acoustical zone-centre modes:

$$\begin{aligned}\Gamma = {} & \underbrace{2A_{1g} \oplus 4B_{1g} \oplus B_{2g} \oplus 5E_g}_{\text{Raman}} \oplus \underbrace{3A_{2u} \oplus 4E_u}_{\text{IR}} \oplus \underbrace{A_{2u} \oplus E_u}_{\text{Acoustic}} \\ & \oplus \underbrace{B_{1u} \oplus A_{2g} \oplus A_{1u} \oplus 2B_{2u}}_{\text{Silent}} .\end{aligned}$$

Because of the non-vanishing components of the Born effective charge tensors, the dipole–dipole interaction must be properly included in the calculation of the interatomic force constants [7, 32, 33]. In particular, the dipole–dipole contribution is found to be responsible for the splitting between the longitudinal and transverse optic (LO and TO, respectively) modes E_u (perpendicular to c) and A_{2u} (parallel to c) at the Γ point.

In table 4.5.9, the calculated phonon frequencies are compared with experimental values. For hafnon, experimental data are only available for Raman modes, in the form of two sets of measurements [59, 60]. Since the agreement with both sets of data is excellent, we report here only the most recent data [60]. For zircon, both Raman and IR-active modes have been studied experimentally [61], the IR data being confirmed by more recent experiments [62, 63].

Overall, the agreement between theory and experiment is excellent, with an rms absolute deviation of $4.1\,\mathrm{cm}^{-1}$ for $HfSiO_4$ ($9.4\,\mathrm{cm}^{-1}$ for $ZrSiO_4$), and an rms relative deviation of 4.2% (2.5%). We obtain four Raman active

Table 4.5.9. Fundamental frequencies of $HfSiO_4$ and $ZrSiO_4$ (in cm^{-1}) with their symmetry assignments.

	$HfSiO_4$		$ZrSiO_4$	
Mode	Theoretical	Experimental	Theoretical	Experimental
Raman				
$A_{1g}(1)$	462	450	442	439
$A_{1g}(2)$	970	984	971	974
$B_{1g}(1)$	162	157	225	214
$B_{1g}(2)$	395	401	397	393
$B_{1g}(3)$	638	620	632	–
$B_{1g}(4)$	1016	1020	1017	1008
B_{2g}	247	267	252	266
$E_g(1)$	161	148	194	201
$E_g(2)$	204	212	225	225
$E_g(3)$	369	351	375	357
$E_g(4)$	530	–	536	547
$E_g(5)$	923	–	923	–
Infrared				
A_{2u} (TO1)	312		348	338
A_{2u} (LO1)	423		476	480
A_{2u} (TO2)	598		601	608
A_{2u} (LO2)	656		646	647
A_{2u} (TO3)	983		980	989
A_{2u} (LO3)	1095		1096	1108
E_u (TO1)	252		285	287
E_u (LO1)	313		341	352
E_u (TO2)	395		383	389
E_u (LO2)	409		420	419
E_u (TO3)	420		422	430
E_u (LO3)	461		466	471
E_u (TO4)	873		867	885
E_u (LO4)	1023		1029	1035
Silent				
B_{1u}	107		120	
A_{2g}	233		242	
A_{1u}	383		392	
$B_{2u}(1)$	573		566	
$B_{2u}(2)$	945		943	

The experimental values are taken from [60] for $HfSiO_4$ (Raman modes only), and from [61] for $ZrSiO_4$.

modes that could not be detected experimentally: two for hafnon (at 530 cm^{-1} [$E_g(4)$] and 923 cm^{-1} [$E_g(5)$]) and two for zircon (at 632 cm^{-1} [$B_{1g}(3)$] and 923 cm^{-1} [$E_g(5)$]).

We also obtain silent modes, inactive for both IR and Raman experiments. They are found to range from 107 to 945 cm^{-1} in $HfSiO_4$, and from 120 to 943 cm^{-1} in $ZrSiO_4$. Two of these (B_{1u} and A_{2g}) are very soft, and correspond, in a first approximation, to vibration modes in which the SiO_4 tetrahedra rotate as a unit [61] (in the u and g modes the tetrahedra move with opposite phases).

In the 'Phonon frequencies at the Γ point' section, we pointed out three origins for the variations of the frequencies in Hf- and Zr-based oxides: the structural changes, the mass ratio Hf/Zr equal to 1.96 and the differences in interatomic force constants. It is quite interesting to compare on the same basis the phonon frequencies calculated for $HfSiO_4$ and $ZrSiO_4$ (see table 4.5.9).

By performing a similar analysis as for HfO_2 versus ZrO_2, we find that the structural changes play a very minor role, in agreement with the intuition resulting from the very small variations observed in table 4.5.7. The effect of the mass ratio is clear for the $B_{1g}(1)$ mode in which the M = (Hf, Zr) atoms move significantly more than O atoms: the frequency increases by about 28% in $ZrSiO_4$. In contrast, the frequencies should not vary much from $HfSiO_4$ to $ZrSiO_4$ for modes in which the M = (Hf, Zr) atoms are not involved (i.e. all the silent modes, $A_{1g}(1)$ and (2), and B_{2g}), as well as for those in which the O atoms move significantly more than the M = (Hf, Zr) atoms. In most of these cases, this is indeed what is observed; in a few cases, however, the differences in the interatomic force constants dominate, e.g., for the B_{1u} mode for which the frequency increases by about 11%.

Dielectric permittivity tensors

Due to the tetragonal symmetry of the hafnon and zircon crystals, the electronic (ϵ_∞) and static (ϵ_0) permittivity tensors have two independent components $\epsilon_\parallel$ and $\epsilon_\perp$ parallel and perpendicular to the c-axis, respectively. The calculated values of ϵ_∞ and ϵ_0 are reported in table 4.5.10.

For zircon, values of 10.69 (3.8) [62] and 11.25 (3.5) [63] are reported for the static (electronic) dielectric permittivity in the directions parallel and perpendicular to the tetragonal axis, respectively. Our theoretical values are larger than the experimental ones by about 10%, as often found in the LDA to DFT. For hafnon, we were not able to find accurate measurements in the literature: for hafnium silicates, values ranging from 11 to 25 have been reported.

The contribution of the individual modes $\Delta\epsilon_m$ to the static dielectric constant, as defined in equation (4.5.13), is also indicated in table 4.5.10. The largest contribution comes from the lowest frequency mode. The

Table 4.5.10. Electronic and static dielectric tensors of $HfSiO_4$ and $ZrSiO_4$.

	$HfSiO_4$		$ZrSiO_4$	
	$\parallel$	$\perp$	$\parallel$	$\perp$
ϵ_∞	4.11	3.88	4.26	4.06
$\Delta\epsilon_1$	4.93	4.38	5.90	5.16
$\Delta\epsilon_2$	0.81	0.75	0.52	1.31
$\Delta\epsilon_3$	0.80	0.35	0.85	0.05
$\Delta\epsilon_4$		1.27		1.38
ϵ_0	10.65	10.63	11.53	11.96

The contributions of individual phonon modes to the static dielectric tensor are indicated. The tensors are diagonal and have different components parallel (||) and perpendicular (⊥) to the *c*-axis. The phonon mode contributions to $\epsilon_0^{\parallel}$ come from the three IR-active A_{2u} modes, while the contributions to $\epsilon_0^{\perp}$ come from the four IR-active E_u modes.

decomposition of the static dielectric tensor can further be analysed using the mode-effective charge vectors and the oscillator strength tensors, defined by equations (4.5.12) and (4.5.14), respectively. In table 4.5.11, we present, for each IR-active mode, the magnitude of its mode-effective charge vectors (this vector is parallel and perpendicular to the tetragonal axis for A_{2u} and E_u modes, respectively), as well as the relevant component of the oscillator strength tensor (the parallel–parallel component for A_{2u} modes, and the perpendicular–perpendicular component for E_u modes).

Table 4.5.11. Components of mode-effective charge vectors Z_m^* and oscillator strength tensor S_m for each of the IR-active modes for $HfSiO_4$ and $ZrSiO_4$.

	$HfSiO_4$		$ZrSiO_4$	
	Z_m^*	S_m	Z_m^*	S_m
$A_{2u}(1)$	6.85	7.39	7.68	10.06
$A_{2u}(2)$	3.78	4.24	2.76	2.64
$A_{2u}(3)$	6.60	11.22	6.71	11.50
$E_u(1)$	5.93	4.05	6.79	5.91
$E_u(2)$	2.94	1.70	3.51	2.71
$E_u(3)$	1.69	0.91	0.28	0.12
$E_u(4)$	7.21	14.02	7.37	14.69

The description of the reported vector and tensor components corresponding to the two types of mode is given in the text. The components of the mode-effective charge vectors are given in units of $|e|$, where e is the electronic charge. The oscillator strengths are given in 10^{-4} atomic units ($1\,\text{a.u.} = 0.342\,036\,\text{m}^3\,\text{s}^{-2}$).

For each symmetry representation (A_{2u} and E_u), the lowest- and highest-frequency modes exhibit the largest effective charges and the largest oscillator strengths. Despite their similar oscillator strengths, the modes of lowest frequency contribute much more to the static dielectric constant than the modes of highest frequency, the frequency factor in equation (4.5.13) playing a crucial role. The second-lowest-frequency modes are moderately strong, while the third E_u modes have a negligible IR activity.

Similarly to what was observed when comparing hafnia and zirconia (see the 'Dielectric permittivity tensors' section), the oscillator strengths and the mode-effective charges are smaller for $HfSiO_4$ than for $ZrSiO_4$ (except for the $A_{2u}(2)$ and $E_u(3)$ modes). The origin of this difference can be traced back to the Born effective charges and the eigendisplacements. Indeed, as discussed in the 'Born effective charge tensors' section, the Born effective charges of M = (Hf, Zr) and Si atoms are smaller in $HfSiO_4$ than in $ZrSiO_4$. Moreover, due to their heavier weight, the displacements of Hf atoms are smaller than those of Zr atoms.

Coming back to the contributions to the static dielectric constant reported in table 4.5.10, we observe that most of the contributions for $HfSiO_4$ are smaller than those for $ZrSiO_4$ (except those of the $A_{2u}(2)$ and $E_u(3)$ modes). In the cases where the oscillator strengths are smaller for hafnon than for zircon, the behaviour of the phonon frequencies will also influence the contribution to ϵ_0. Indeed, when the corresponding frequency in $HfSiO_4$ is higher than in $ZrSiO_4$, the contribution to the static dielectric constant is further increased (as for the $E_u(2)$ modes). In contrast, when the frequency is lower, the difference in the contribution is lower than in the oscillator strength. For instance, for the $A_{2u}(1)$ mode, the oscillator strength S_m in hafnon is 30% smaller than in zircon, but the corresponding contribution to ϵ_0 is only 20% smaller, since the associated frequency is about 10% larger. Finally, for the $A_{2u}(2)$ and $E_u(3)$ modes, the frequencies are very similar (these modes essentially involve displacements of the Si atoms and of some of the O atoms) and therefore the oscillator strength governs the trend of the contributions to the static dielectric constant (larger in hafnon than in zircon).

Amorphous silicates

The dielectric properties of Zr and Hf amorphous silicates constitute an issue of great practical importance. Early experimental measurements suggested a supralinear dependence of the static dielectric constant ϵ_0 on the M = (Hf, Zr) concentration [64]. While several phenomenological theories addressed this behaviour [65, 66], more recent data appear to favour instead a close to linear dependence [67, 68]. In a recent paper [69], we have used DFT simulations to shed some light on this particularly relevant issue by investigating how the permittivity of Zr silicates is affected by the underlying nanoscopic structure.

In tackling this technological problem, we face the more general issue of predicting the dielectric properties of amorphous alloys from first principles. Brute force analysis of numerous large supercells is beyond present computational capabilities. To overcome this difficulty, we establish a relationship between the dielectric properties of Zr silicates and their underlying nanoscopic structure. Using DFT, we compute optical and static dielectric constants for various model structures of Zr silicates, both ordered and disordered. We introduce a scheme which relates the dielectric constants to the local bonding of Si and Zr atoms. This scheme is based on the definition of parameters characteristic of the basic SUs formed by Si and Zr atoms and their nearest neighbours.

Applied to amorphous Zr silicates, our scheme provides a good description of measured dielectric constants, both optical [68, 70] and static [67, 68], and reveals the important contribution of ZrO_6 SUs to the static dielectric constant. In a very similar way, our scheme can also be used to investigate Hf silicates. Only here we briefly indicate how the two systems compare.

We consider model structures of $(ZrO_2)_x(SiO_2)_{1-x}$, nine crystalline and one amorphous, with x ranging from 0 to 0.5, and describe them in terms of cation-centred SUs. We start with three different SiO_2 polymorphs ($x = 0$):

[C_0] α-cristobalite with four SiO_4 SUs per unit cell
[Q_0] α-quartz with three SiO_4 SUs
[S_0] stishovite with two SiO_6 SUs

By substituting one of the Si atoms by a Zr atom for each of these models, we generate three new crystal structures:

[C_1] Zr^{Si} in α-cristobalite with three SiO_4 and one ZrO_4 SUs per unit cell ($x = 0.25$)
[Q_1] Zr^{Si} in α-quartz with two SiO_4 and one ZrO_4 SUs ($x = 0.33$)
[S_1] Zr^{Si} in stishovite with one SiO_6 and one ZrO_6 SUs

We also consider zircon, as well as two other structures generated by replacing Zr by Si:

[Z_2] zircon that contains two SiO_4 and two ZrO_8 SUs per unit cell ($x = 0.5$)
[Z_1] Si^{Zr} in zircon with two SiO_4, one SiO_6 and one ZrO_8 SUs ($x = 0.25$)
[Z_0] fully Si-substituted zircon with two SiO_4 and SiO_6 SUs ($x = 0$)

Finally, the amorphous structure [A] is generated using classical molecular dynamics with empirical potentials [69]. In this study, only a single disordered structure could be afforded because of the noticeable computational cost associated.

The atomic coordinates and the cell parameters of all our model structures are fully relaxed within the LDA to DFT. The calculated optical and static dielectric constants for our model structures are given in table 4.5.12. Due to the well-known limitations of the LDA, the theoretical values are larger than the experimental ones (when available) by about 10%.

In order to understand how the optical dielectric constant (ϵ_∞) depends on the underlying atomic nanostructure, we consider the electronic polarizability $\bar{\alpha}$ which is related to ϵ_∞ by the Clausius–Mosotti relation [66, 68]:

$$\frac{\epsilon_\infty - 1}{\epsilon_\infty + 2} = \frac{4\pi}{3}\frac{\bar{\alpha}}{\bar{V}} \tag{4.5.16}$$

where $\bar{V}$ is the average SU volume. The polarizability $\bar{\alpha}$ can be taken as a local and additive quantity, in contrast with ϵ_∞. Therefore, we define α_i values for each SU i, where $i \equiv \mathrm{SiO}_n$ (with $n = 4$ or 6) or ZrO_n (with $n = 4$, 6 or 8), such that:

$$\bar{\alpha} = \sum_i x_i \alpha_i, \tag{4.5.17}$$

where x_i is the molecular fraction. In table 4.5.13, we report the five α_i values that we obtain by solving in a least-squares sense the over-determined system based on the calculated ϵ_∞ values for the nine crystalline models. The optical dielectric constants derived from these α_i values using equations (4.5.16) and (4.5.17) compare well with those calculated from first principles, showing average and maximal errors smaller than 1 and 2.5%, respectively. For the amorphous model, which was not used to determine the α_i values, the derived value $\epsilon_\infty = 3.25$ is in excellent agreement with the first-principles

Table 4.5.12. Composition (x), optical (ϵ_∞) and static (ϵ_0) dielectric constants, volume ($\bar{V}$) in bohr^3, polarizability $\bar{\alpha}$ in bohr^3, characteristic dynamical charge ($\bar{Z}$), and characteristic force constant ($\bar{C}$) in hartree/bohr^2 for the various model systems.

Model	x	ϵ_∞	ϵ_0	$\bar{V}$	$\bar{\alpha}$	$\bar{Z}$	$\bar{C}$
C_0	0.00	2.38	4.30	264.77	19.92	4.21	0.4391
C_1	0.25	2.76	5.25	273.21	24.12	4.59	0.3895
Q_0	0.00	2.54	4.83	240.34	19.46	4.28	0.4169
Q_1	0.33	2.91	5.84	275.28	25.56	4.85	0.3661
S_0	0.00	3.36	10.33	153.74	16.16	4.81	0.2716
S_1	0.50	4.44	24.20	201.88	25.74	6.14	0.1188
Z_0	0.00	3.37	10.11	167.80	17.68	4.76	0.2512
Z_1	0.25	3.94	18.36	189.74	22.42	5.29	0.1287
Z_2	0.50	4.13	11.81	213.28	26.00	5.58	0.2385
A	0.15	3.24	8.92	213.12	21.75	4.83	0.2424

The reported dielectric constants correspond to orientational averages.

Table 4.5.13. Polarizability (α in bohr^3), characteristic dynamical charge (Z) and characteristic force constant (C in hartree/bohr^2) for various SUs.

	SiO_4	SiO_6	ZrO_4	ZrO_6	ZrO_8
α	19.68	16.14	37.37	35.35	32.69
Z	4.29	4.92	5.66	7.16	6.73
C	0.3597	0.2176	0.4202	0.0817	0.1153

result $\epsilon_\infty = 3.24$. These results justify *a posteriori* the use of equations (4.5.16) and (4.5.17) to model the optical dielectric constant.

For the static dielectric constant (ϵ_0), the phonon contributions preclude a description in terms of a single local and additive quantity as the electronic polarizability. To overcome this difficulty, we focus on the difference between dielectric constants ($\Delta\epsilon$):

$$\Delta\epsilon = \epsilon_0 - \epsilon_\infty = \frac{4\pi}{\Omega_0}\sum_m \frac{S_m}{\omega_m^2} = \frac{4\pi}{\bar{V}}\frac{\bar{Z}^2}{\bar{C}}, \tag{4.5.18}$$

where ω_m and S_m are the frequency and the oscillator strength of the mth mode. The volume of the primitive unit cell Ω_0 is related to the volume $\bar{V}$ and to the number of SUs $\bar{N}$ by $\Omega_0 = \bar{N}\bar{V}$. The characteristic dynamical charge $\bar{Z}$ and characteristic force constant $\bar{C}$ are defined by:

$$\bar{Z}^2 = \frac{1}{\bar{N}}\sum_\kappa Z_\kappa^2 \quad \text{and} \quad \bar{C}^{-1} = \frac{1}{\bar{N}}\sum_m \frac{S_m}{\omega_m^2 \bar{Z}^2}, \tag{4.5.19}$$

where Z_κ are the atomic Born effective charges.

The variation of $\Delta\epsilon$ due to a Si → Zr substitution has been analysed in detail in [69], where the contribution from sixfold-coordinated atoms has been highlighted. In fact, these configurations resemble those in ABO_3 perovskites. The enhancement of $\Delta\epsilon$ originates from very low-frequency modes in which the cations (A or B) move in opposition with the O atoms while carrying opposite effective charges.

By analogy with the polarizability, we define Z_i and C_i values for each SU such that:

$$\bar{Z}^2 = \sum_i x_i Z_i^2 \quad \text{and} \quad \bar{C}^{-1} = \sum_i x_i C_i^{-1}, \tag{4.5.20}$$

though the locality and the additivity of these parameters is not guaranteed *a priori*. We determine the optimal values Z_i and C_i in the same way as for α_i (table 4.5.13).

For the nine crystalline models, the values of $\Delta\epsilon$ obtained by introducing these parameters in equations (4.5.18) and (4.5.20) match quite well with those calculated from first principles [69], though the agreement is not as impressive as for ϵ_∞. Differences result primarily from the determination of $\bar{C}$. By contrast, the values of $\bar{Z}$ given by equation (4.5.20) agree very well with those computed from first principles, showing an average and maximal error smaller than 2 and 3%, respectively. *A posteriori*, $\bar{C}$ appears to be less local and additive. In fact, it can be demonstrated that the locality of $\bar{C}$ is closely related to the dynamical charge neutrality of the SUs [69].

For the amorphous model, which was not used to determine the Z_i and C_i values, the agreement between the model and the first-principles $\Delta\epsilon$ is excellent with an error smaller than 1% [69]. Indeed, our scheme is more accurate for disordered systems, where the localization of vibrational modes is enhanced and the dynamical charge neutrality appears better respected.

For Zr silicates of known composition in terms of SUs, the parameters in table 4.5.13 fully determine the dielectric constants. Several points are noteworthy. First, the three parameters of Zr-centred SUs all contribute to enhancing the dielectric constants over those of Si-centred ones of corresponding coordination[1]. This is clearly at the origin of the increase of ϵ_∞ and ϵ_0 with increasing Zr concentration. Second, while the polarizability α_i of a given SU (Si or Zr centred) steadily decreases with increasing coordination, such a regular behaviour is not observed for the parameters Z_i and C_i determining $\Delta\epsilon$. In fact, Z_i and C_i concurrently vary to enhance the contribution of ZrO_6 units, which are the SUs giving the largest contribution to $\Delta\epsilon$ in amorphous Zr silicates.

Based on the scheme given by equations (4.5.16)–(4.5.20), we can now estimate ϵ_∞ and ϵ_0 for amorphous $(ZrO_2)_x(SiO_2)_{1-x}$ as a function of Zr composition ($0 < x < 0.5$). Using measured densities for Zr silicates [70], we first obtain ϵ_∞ as a function of x. As shown in figure 4.5.4, our theoretical values[2] are in excellent agreement with available experimental data [68, 70].

To apply our scheme for $\Delta\epsilon$, we need additional information on the cationic coordination. We take the Si atoms to be fourfold coordinated. The coordination of Zr atoms is less well determined. Recent EXAFS measurements [65] indicate that the average Zr coordination grows from about four to about eight for Zr concentrations increasing from $x \sim 0$ to $x \sim 0.5$. In figure 4.5.4, we report calculated ϵ_0 for amorphous $(ZrO_2)_x(SiO_2)_{1-x}$ as a function of x, together with the available experimental data [64, 67, 68, 71].

---

[1] In table 4.5.13, the value of C for SiO_4 apparently leads to a higher contribution to $\Delta\epsilon$ than that for ZrO_4. This is an artifact of the approach we used to determine the Z_i and C_i.

[2] Because the various Zr-centred units have close α values compared to SiO_4 (table 4.5.13), the effect of Zr coordination on ϵ_∞ is negligible.

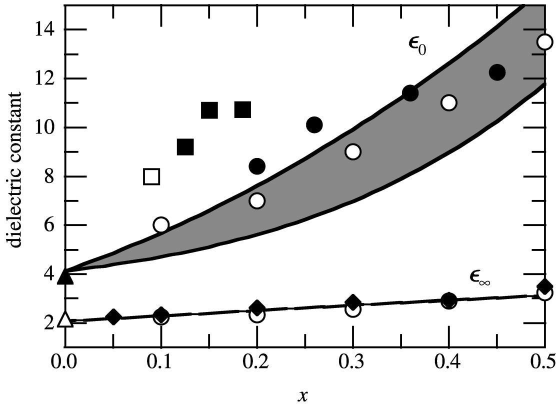

Figure 4.5.4. Dielectric constants (ϵ_∞ and ϵ_0) as a function of composition x for amorphous $(ZrO_2)_x(SiO_2)_{1-x}$. The grey region corresponds to results derived from our model scheme and reflects the indetermination of the number of ZrO_6 units. The upper curve delimiting the band corresponds to structures entirely composed of ZrO_6 units, while the lower curve represents a smooth transition from a structure composed of ZrO_4 units at $x = 0$ to one composed of ZrO_8 units at $x = 0.5$, without the occurrence of any ZrO_6 units. The references for the experimental data are: ◆ [70], ● [67], ○ [68], ■ [64], □ [71], ▲ [72] and △ [73].

The theoretical results are given in the form of a band reflecting the indetermination of the coordination of Zr atoms. We modelled the dielectric constant in terms of suitable distributions of three representative SUs (ZrO_4, ZrO_6 and ZrO_8). The upper curve delimiting the band in figure 4.5.4 corresponds to structures entirely composed of ZrO_6 units. The lower curve is for amorphous systems which do not contain any ZrO_6 units. The average Zr coordination varies linearly from four to eight between $x = 0$ and $x = 0.5$, with concentrations of ZrO_4 and ZrO_8 SUs varying at most quadratically. Note that the upper part of the band agrees well with the recent experimental data [67, 68]. The earlier data [64, 71] cannot be explained. Figure 4.5.4 shows that, for a sufficient number of ZrO_6 units, values of ϵ_0 at intermediate x can indeed be larger than estimated from a linear interpolation between SiO_2 and $ZrSiO_4$. However, in accord with recent experiments [67, 68], our theory indicates that the extent of this effect is more limited than previously assumed [64, 65].

Our scheme could also be applied to Hf silicates which are very similar to Zr silicates. In this respect, the comparison between $HfSiO_4$ and $ZrSiO_4$ carried out in the 'Crystalline silicates' section is very useful. Translated in terms of the quantities defined in this section, we get $\bar{V} = 220.13$, $\bar{\alpha} = 25.74$, $\bar{Z} = 5.50$ and $\bar{C} = 0.2581$ for hafnon to be compared with $\bar{V} = 213.28$, $\bar{\alpha} = 26.00$, $\bar{Z} = 5.58$ and $\bar{C} = 0.2385$ for zircon. Basically, all these parameters show a similar trend that leads to smaller dielectric permittivities (both electronic and static) for hafnon than for zircon. For amorphous Hf silicates, we expect the same kind of consideration to apply.

Conclusions

Using DFT, we have investigated the structural, electronic, dynamical and dielectric properties for a series of high-κ materials belonging to the Hf–Si–O and Zr–Si–O systems. We have considered hafnia and zirconia (the crystalline oxides), hafnon and zircon (the crystalline silicates) and finally the amorphous silicates.

In all the investigated systems, the parameters of the relaxed atomic structures are found to be in very good agreement with experimental ones (when available). The phonon frequencies at the centre of the Brillouin zone, the Born effective charge tensors, and the dielectric permittivity tensors have been obtained using density-functional perturbation theory.

For the crystalline systems, we have found an excellent agreement between the calculated phonon frequencies and their corresponding experimental values. For hafnia and zirconia, both the cubic and the tetragonal phases have been investigated. For t-ZrO_2, we have proposed new symmetry assignments that meet all the arguments discussed in the literature. Our assignments solve the apparent contradictions of previous works, clarifying some important issues. We have also illustrated the relationship between the phonon modes of the cubic and the tetragonal phases. In all the cases, the differences between the Hf- and Zr-based systems have been analysed in detail and interpreted in terms of structural changes, the mass ratio and variations of interatomic force constants.

An important anisotropy was observed in the Born effective charge tensors. For some directions, these effective charges are found to be larger than the nominal ionic charge, indicating a mixed covalent–ionic bonding between M = (Hf, Zr) and O atoms, and between Si and O atoms. We have also discussed the effective charges focusing on the changes between the systems containing hafnium and those containing zirconium.

The electronic and static dielectric permittivity constants have been computed, and a detailed analysis of the contributions of individual vibrational modes has been performed, including the computation of mode-effective charges and oscillator strengths. For the tetragonal systems (t-HfO_2, t-ZrO_2, $HfSiO_4$ and $ZrSiO_4$), we observed, for directions both parallel and perpendicular to the tetragonal axis, that a single mode contributes for more than 60% of the full ionic contribution. Our first-principles approach allows us to obtain the corresponding eigenvectors, showing clearly that the displacement is characterized by Zr and O atoms moving in opposite directions. In the silicates, the displacement of Si atoms in these modes is less than half those of the other species, inducing a substantial distortion of the SiO_4 tetrahedra in contradiction to what was previously thought. For all systems, the modifications related to the presence of Zr rather than Hf have been rationalized in terms of the difference in mass between these atoms, variations of interatomic force constants and changes in structural parameters (minor effect).

For hafnon and zircon, we have also calculated the electronic DOS in which the contributions from Hf 5s and 5p, Zr 4s and 4p and O 2s and 2p are clearly distinguishable, although the spread of the latter indicates hybridization with atomic M = (Hf, Zr) and Si orbitals.

Finally, we have investigated the dielectric properties of amorphous silicates. We have provided a simple scheme which relates the optical and static dielectric constants of Zr silicates to their underlying nanoscopic structure. Our theory supports recent experiments which find a close to linear dependence of ϵ_0 on the Zr fraction x, and shows that higher dielectric constants can be achieved by increasing the concentration of ZrO_6 SUs. For Hf silicates, we expect a very similar behaviour based on the comparison made throughout this chapter.

Acknowledgments

We thank F. Detraux and A. Bongiorno who took an active part in the research leading to the results presented in this chapter. We are also grateful to R.B. van Dover for providing us his results prior to publication. Support is acknowledged from the FNRS-Belgium (G.-M.R. and X.G.), the Swiss FNS under grant No 620-57850.99 (A.P.), the FRFC project (No 2.4556.99), the Belgian PAI-5/1/1 and the Swiss Center for Scientific Computing.

References

[1] Hohenberg P and Kohn W 1964 *Phys. Rev.* **136** B864–B871
[2] Kohn W and Sham L J 1965 *Phys. Rev.* **140** A1133–A1138
[3] Pickett W 1989 *Comput. Phys. Rep.* **9** 115–197
[4] Payne M C, Teter M P, Allan D C, Arias T A and Joannopoulos J D 1992 *Rev. Mod. Phys.* **64** 1045–1097
[5] Baroni S, de Gironcoli S, Dal Corso A and Giannozzi P 2001 *Rev. Mod. Phys.* **73** 515–562
[6] Gonze X 1997 *Phys. Rev. B* **55** 10337–10354
[7] Gonze X and Lee C 1997 *Phys. Rev. B* **55** 10355–10368
[8] Gonze X *et al* 2002 *Comput. Mater. Sci.* **25** 478–492 http://www.abinit.org
[9] Perdew J P and Wang Y 1992 *Phys. Rev. B* **45** 13244–13249
[10] Ceperley D M and Alder B J 1980 *Phys. Rev. Lett.* **45** 566–569
[11] Troullier N and Martins J L 1991 *Phys. Rev. B* **43** 1993–2006
[12] Teter M P 1993 *Phys. Rev. B* **48** 5031–5041

[13] Weast R C (ed) 1985 *Handbook for Chemistry and Physics* 65th edn (Boca Raton, FL: CRC Press) p 165

[14] Ruh R and Corfield P W R 1970 *J. Am. Ceram. Soc.* **53** 126–129

[15] Little E J and Jones M M 1960 *J. Chem. Educ.* **37** 231

[16] Duran P and Pascual C 1984 *J. Mater. Sci.* **19** 1178–1184

[17] Teufer G 1962 *Acta Cryst.* **15** 1187

[18] Ruh R, Garrett H J, Domagala R F and Tallen N M 1968 *J. Am. Ceram. Soc.* **51** 23

[19] Aldebert P and Traverse J P 1985 *J. Am. Ceram. Soc.* **68** 34–40

[20] Perry C H, Liu D W and Ingel R P 1985 *J. Am. Ceram. Soc.* **68** C184–C187

[21] Lawson S 1995 *J. Eur. Ceram. Soc.* **15** 485–502

[22] Hunter O Jr, Scheidecker R W and Tojo S 1979 *Ceram. Int.* **5** 137

[23] Kráĺik B, Chang E K and Louie S G 1998 *Phys. Rev. B* **57** 7027–7036

[24] Rignanese G-M, Detraux F, Gonze X and Pasquarello A 2001 *Phys. Rev. B* 13430 **64** 1–7

[25] Demkov A A 2001 *Phys. Status Solidi B* **226** 57–67

[26] Zhao X and Vanderbilt D 2002 *Phys. Rev. B* 233106 **65** 1–4

[27] Zhao X and Vanderbilt D 2002 *Phys. Rev. B* 075105 **65** 1–10

[28] Wang J, Li H P and Stivens R 1992 *J. Mater. Sci.* **27** 5397–5430

[29] Zhong W, King-Smith D and Vanderbilt D 1994 *Phys. Rev. Lett.* **72** 3618–3621

[30] Lee C and Gonze X 1994 *Phys. Rev. Lett.* **72** 1686–1689

[31] Lee C, Ghosez Ph and Gonze X 1994 *Phys. Rev. B* **50** 13379–13387

[32] Gonze X, Charlier J-C, Allan D C and Teter M P 1994 *Phys. Rev. B* **50** 13035–13038

[33] Giannozzi P, de Gironcoli S, Pavone P and Baroni S 1991 *Phys. Rev. B* **43** 7231–7242

[34] Feinberg A and Perry C H 1981 *J. Phys. Chem. Solids* **42** 513–518

[35] Ishigame M and Sakurai T 1977 *J. Am. Ceram. Soc.* **60** 367–369

[36] Kim D-J, Jung H-J and Yang I-S 1993 *J. Am. Ceram. Soc.* **76** 2106–2108

[37] Hirata T, Asari E and Kitajima M 1994 *J. Solid State Chem.* **110** 201–207

[38] Kjerulf-Jensen N, Berg R W and Poulsen F W 1996 *Proc. 2nd European Solid Oxide Fuel Cell Forum* (Oberrohrdorf, Switzerland: U. Bossel) pp 647–656

[39] Pecharromán C, Ocaña M and Serna C J 1996 *J. Appl. Phys.* **80** 3479–3483

[40] Mirgorodsky A P, Smirnov M B and Quintard P E 1997 *Phys. Rev. B* **55** 19–22

[41] Mirgorodsky A P, Smirnov M B and Quintard P E 1999 *J. Phys. Chem. Solids* **60** 985–992

[42] Bouvier P and Lucazeau G 2000 *J. Phys. Chem. Solids* **61** 569–578

[43] Liu D W, Perry C H and Ingel R P 1988 *J. Appl. Phys.* **64** 1413–1417

[44] Philippi C M and Mazdiyasni K S 1971 *J. Am. Ceram. Soc.* **54** 254–258

[45] Pecharromán C and Iglesias J E 1994 *Phys. Rev. B* **49** 7137–7147

[46] Kukli K, Ihanus J, Ritala M and Leskela M 1996 *Appl. Phys. Lett.* **68** 3737–3739

[47] Gusev E P, Cartier E, Buchanan D A, Gribelyuk M, Copel M, Okorn-Schmidt H and D'Emic C 2001 *Microelectron. Eng.* **59** 341–349

[48] Wood D L and Nassau K 1982 *Appl. Opt.* **12** 2978–2981

[49] French R H, Glass S J, Ohuchi F S, Xu Y-N and Ching W Y 1994 *Phys. Rev. B* **49** 5133–5142

[50] Lanagan M T, Yamamoto J K, Bhalla A and Sankar S G 1989 *Mater. Lett.* **7** 437–440

[51] Dwivedi A and Cormack A N 1990 *Philos. Mag.* **61** 1–22

[52] Negita K 1989 *Acta Metall.* **37** 313–317

[53] Negita K and Takao H 1989 *J. Phys. Chem. Solids* **50** 325–331

[54] Speer J A and Cooper B J 1982 *Am. Mineral.* **67** 804–808

[55] Rignanese G-M, Gonze X and Pasquarello A 2001 *Phys. Rev. B* 104305 **63** 1–7
[56] Mursic Z, Vogt T, Boysen H and Frey F 1992 *J. Appl. Crystallogr.* **25** 519–523
[57] Ghosez Ph, Michenaud J-P and Gonze X 1998 *Phys. Rev. B* **58** 6224–6240
[58] Gonze X, Allan D C and Teter M P 1992 *Phys. Rev. Lett.* **68** 3603–3606
[59] Nicola J H and Rutt H N 1974 *J. Phys. C: Solid State Phys.* **7** 1381–1386
[60] Hoskin P W O and Rodgers K A 1996 *Eur. J. Solid State Inorg. Chem.* **23** 1111–1121
[61] Dawson P, Hargreave M M and Wilkinson G R 1971 *J. Phys. C: Solid State Phys.* **4** 240–256
[62] Gervais F, Piriou B and Cabannes F 1973 *J. Phys. Chem. Solids* **34** 1785–1796
[63] Pecharromán C, Ocaña M, Tartaj P and Serna C J 1994 *Mater. Res. Bull.* **29** 417–426
[64] Wilk G D and Wallace R M 2000 *Appl. Phys. Lett.* **76** 112–114; Wilk G D, Wallace R M and Anthony J M 2000 *J. Appl. Phys.* **87** 484–492
[65] Lucovsky G and Rayner G B Jr 2000 *Appl. Phys. Lett.* **77** 2912–2914
[66] Kurtz H A and Devine R A B 2001 *Appl. Phys. Lett.* **79** 2342–2344
[67] Qi W-J, Nieh R, Dharmarajan E, Lee B H, Jeon Y, Kang L, Onishi K and Lee J C 2000 *Appl. Phys. Lett.* **77** 1704–1706
[68] van Dover R B, Manchanda L, Green M L, Wilk G, Garfunkel E and Busch B unpublished
[69] Rignanese G M, Detraux F, Gonze X, Bongiorno A and Pasquarello A 2002 *Phys. Rev. Lett.* 117601 **89** 1–4
[70] Nogami M 1985 *J. Non-Cryst. Solids* **69** 415–423
[71] Misra V unpublished
[72] Varshneya A K 1994 *Fundamental of Inorganic Glasses* (San Diego, CA: Academic) p 364
[73] Weast R C (ed) 1972 *Handbook of Chemistry and Physics*, 52nd edn (Cleveland, OH: Chemical Rubber Co.) p E-204